



Meshfree modeling of concrete slab perforation using a reproducing kernel particle impact and penetration formulation



Jesse A. Sherburn^{a,*}, Michael J. Roth^a, J.S. Chen^b, Michael Hillman^b

^a U.S. Army Engineer Research and Development Center, Vicksburg, MS, USA

^b Department of Structural Engineering, University of California San Diego, San Diego, CA, USA

ARTICLE INFO

Article history:

Received 24 October 2014

Received in revised form

17 June 2015

Accepted 10 July 2015

Available online 26 July 2015

Keywords:

Reproducing kernel particle method

Meshfree

Concrete

Penetration

Damage mechanics

ABSTRACT

A meshfree formulation under the reproducing kernel particle method (RKPM) was introduced for modeling the penetration and perforation of brittle geomaterials such as concrete. RKPM provides a robust framework to effectively model the projectile-target interaction and the material failure and fragmentation behaviors that are critical for this class of problems. A stabilized semi-Lagrangian formulation, in conjunction with a multiscale material damage model for brittle geomaterials and a kernel contact algorithm, were introduced for penetration modeling. In this work, the accuracy of the meshfree impact and penetration formulation was studied using a series of large-caliber projectile concrete slab perforation experiments with impact velocities in the ballistic regime. These experiments were selected due to the challenging nature of concrete perforation, and the results were used to validate the effectiveness of the proposed method to model the penetration processes and the concrete target failure. Simulation results confirm the formulation's accuracy for this type of high-rate ballistic problem and establish a basis for extension to other types of impact problems. The results show the importance of properly formulating the method of domain integration to maintain accuracy in the presence of concrete fragmentation, and also highlight the method's ability to capture the fragmentation response without a need for non-physical treatments commonly used in conventional methods.

Published by Elsevier Ltd.

1. Introduction

Material and structural response to extreme events like explosive detonation and projectile penetration is an area of significant interest for the military and commercial research communities. The scientific challenges to understand and predict the high-rate and nonlinear response of a diverse range of protective systems necessitates robust methods to effectively model the accompanying complex phenomena. For projectile penetration, the critical failure mechanisms vary depending on projectile velocity, geometry, and material properties of the projectile and target. Primary target failure mechanisms include elastic–plastic cavity expansion, brittle fracture, plugging, fragmentation, and petaling; while penetrators may exhibit large deformation, fracture and hydrodynamic erosion [1]. As a consequence, material response to the high-rate impact loading is a crucial part of the penetration mechanics. For concrete

in particular, the target response is reliant on the pressure dependence of material shear strength, strain softening, and strain localization that leads to material fracture and fragmentation; large secondary debris fields resulting from ejecta in the impact area are common. The ability to accurately model this complex behavior is critical for reliable analysis and optimal design of advanced protective structures.

Following World War II, vast amounts of research emerged on the subject of impact and penetration models [2–9]; numerous comprehensive reviews [e.g., [4,8,9]] are available. Analytical approaches were initially developed, beginning with Bishop et al., in 1945 [2]; cavity expansion models are an important subset and form the basis for a large class of semi-analytical techniques [10–15]. The key shortcoming for these analytical methods is the loss of resolution in the fine-scale physics in order to make the problem tractable. In contrast, numerical methods, if properly validated, provide a more general framework driven by the essential physics. Robustness in the presence of extreme material distortion and failure, however, remains a challenge in computer simulations. Lagrangian structured-mesh methods, like the finite

* Corresponding author. 3909 Halls Ferry Road, Vicksburg, MS 39180, USA. Tel.: +1 601 634 3202.

E-mail address: jesse.a.sherburn@usace.army.mil (J.A. Sherburn).

element method, exhibit mesh sensitivity and subjectivity in the presence of severe material deformation, which is problematic for penetration modeling. Techniques like element erosion [16–18] have been developed as a non-physical treatment; however, issues related to phenomenological failure criteria, contact surface erosion, and contact surface evolution remains. In contrast, while Eulerian finite difference and finite volume methods are more resilient in modeling large deformation and flow [19,20], their fixed grid characteristic generally produces error due to their inability to accurately identify transient contact surfaces and free surface formation. This leads to significant limitations when material breakup is dominant. The constitutive description of materials during high velocity impact is another important aspect of computational penetration mechanics. Material models must address strong strain-rate effects, pressure-dependent shear strength, and the transition from initial damage to material fracture, which is only approximately addressed by phenomenological means. Advancements are being made toward multiscale descriptions of material failure, where behavior is described according to the fundamental mechanics at lower scales [21–25].

Meshfree methods, in contrast to traditional mesh-based methods, do not rely on a structured mesh topology to construct the discrete numerical solution. As a consequence, large deformation and material separation can be naturally captured without requiring the non-physical treatments that are required by other approaches [26,27]. In this work we introduce a meshfree formulation for impact and penetration modeling that is constructed under the framework of the reproducing kernel particle method (RKPM) [28,29]. The formulation is implemented in the nonlinear meshfree analysis program (NMAP) [30], with the purpose of modeling projectile penetration in concrete, where damage and fragmentation dominate the material response. A stabilized semi-Lagrangian formulation is utilized, where particle neighbors evolve with the material deformation and domain integration is accomplished at the particles, i.e., meshfree nodes, with proper stabilization introduced [31–33]. Contact surfaces are defined according to a kernel contact algorithm [34], with the benefit of naturally capturing evolutionary contact surfaces that cannot be defined *a priori*. For the material damage description a multiscale material damage model is implemented [25], where continuum scale damage is linked to microstructure fracture within a rate- and pressure-dependent concrete constitutive model. Using NMAP, the formulation accuracy was studied via two sets of benchmark experiments. First the code was applied to a pair of standard Taylor bar experiments. These simulations were used to verify accuracy and stability of the semi-Lagrangian RKPM with nodal integration technique in the presence of large deformation, which is a prerequisite for the penetration problems that are of primary interest. Following the Taylor bar experiments, the code was applied to a series of concrete perforation experiments, where a large-caliber projectile was used to perforate a set of finite thickness concrete slabs. In these experiments the projectile exit velocity is highly dependent on the projectile-target interaction and an accurate description of the material failure. Results from Taylor bar and penetration simulations were cumulatively used to verify formulation accuracy for this class of strong dynamic problems.

The remainder of this paper is organized in the following manner. An overview of the meshfree impact and penetration formulation is presented in Section 2, which includes the reproducing kernel (RK) approximation, techniques for stable nodal integration with material fracture, a natural kernel contact algorithm, and the multiscale concrete constitute model. The experimental tests (Taylor bar cylinder test and concrete slab penetration) used for validation modeling are discussed in Section 3, and the corresponding numerical models are described in Section 4. Section 5 presents and discusses the simulation results, and Section 6 provides concluding remarks.

2. RKPM formulation for impact and penetration modeling

2.1. Reproducing kernel approximation

In the RKPM framework the solution is approximated using a point-based discretization, where the approximation is formed through overlapping kernels of compact support. Because the kernel construction is not subject to a geometric conformity constraint, mesh dependency in the presence of large distortion is minimized, while a Lagrangian discretization can be used to maintain sharp resolution of material boundaries and interfaces. A key feature of the RK approximation is enforcement of the reproducing conditions. In this way, it serves as a correction of the smoothed particle hydrodynamics [35] approximation, which lacks consistency.

The discrete RK approximation [29] with reference to the material coordinates, \mathbf{X} , is

$$\mathbf{u}^h(\mathbf{X}, t) = \sum_{I=1}^{np} \Psi_I(\mathbf{X}) \mathbf{d}_I(t) \quad (1)$$

where $\mathbf{u}^h(\mathbf{X}, t)$ is the RK approximation of \mathbf{u} , $\Psi_I(\mathbf{X})$ is the RK shape function referenced to the I^{th} node, $\mathbf{d}_I(t)$ is a set of nodal coefficients to be determined, and np is the number of nodes. The RK shape function is constructed as a correction of the compact kernel function, $\phi_a(\mathbf{X} - \mathbf{X}_I)$.

$$\Psi_I(\mathbf{X}) = C(\mathbf{X}; \mathbf{X} - \mathbf{X}_I) \phi_a(\mathbf{X} - \mathbf{X}_I) \quad (2)$$

where continuity and locality are inherited from the kernel function. The correction function, $C(\mathbf{X}; \mathbf{X} - \mathbf{X}_I)$, enforces the reproducibility conditions. A useful attribute in defining the approximation's order of accuracy is that the reproducing condition can be applied to any desired basis (such as monomials or the crack-tip displacement field for fracture mechanics) [36], although pure monomial bases are commonly used. Using a set of n^{th} order complete monomials, the correction function is expressed as

$$C(\mathbf{X}; \mathbf{X} - \mathbf{X}_I) = \sum_{|\alpha|=0}^n (\mathbf{X} - \mathbf{X}_I)^\alpha b_\alpha(\mathbf{X}) = \mathbf{H}^T(\mathbf{X} - \mathbf{X}_I) \mathbf{b}(\mathbf{X}) \quad (3)$$

where $|\alpha| \equiv \alpha_1 + \alpha_2 + \alpha_3$, $(\mathbf{X} - \mathbf{X}_I)^\alpha \equiv (X_1 - X_{1I})^{\alpha_1} (X_2 - X_{2I})^{\alpha_2} (X_3 - X_{3I})^{\alpha_3}$, and $b_\alpha(\mathbf{X}) \equiv b_{\alpha_1 \alpha_2 \alpha_3}(\mathbf{X})$. The n^{th} order complete basis functions are contained in $\mathbf{H}^T(\mathbf{X} - \mathbf{X}_I)$

$$\mathbf{H}^T(\mathbf{X} - \mathbf{X}_I) = [1, (X_1 - X_{1I}), (X_2 - X_{2I}), (X_3 - X_{3I}), (X_1 - X_{1I})^2, \dots, (X_3 - X_{3I})^n] \quad (4)$$

The reproducing conditions

$$\sum_{I=1}^{np} \Psi_I(\mathbf{X}) \mathbf{X}_I^\alpha = \mathbf{X}^\alpha \quad |\alpha| = 0, 1, \dots, n \quad (5)$$

are used to obtain the vector of coefficients, $\mathbf{b}(\mathbf{X}) = \mathbf{M}^{-1}(\mathbf{X})\mathbf{H}(0)$, where $\mathbf{H}^T(0) = [1, 0, \dots, 0]$ and $\mathbf{M}(\mathbf{X})$ is a moment matrix

$$\mathbf{M}(\mathbf{X}) = \sum_{I=1}^{np} \mathbf{H}(\mathbf{X} - \mathbf{X}_I) \mathbf{H}^T(\mathbf{X} - \mathbf{X}_I) \phi_a(\mathbf{X} - \mathbf{X}_I) \quad (6)$$

Consequently, the Lagrangian RK shape function is

$$\Psi_I(\mathbf{X}) = \mathbf{H}^T(\mathbf{X} - \mathbf{X}_I) \mathbf{M}^{-1}(\mathbf{X}) \mathbf{H}(0) \phi_a(\mathbf{X} - \mathbf{X}_I) \quad (7)$$

In the presence of material fracture and fragmentation, mapping between the current and undeformed configurations is no longer one-to-one. As a consequence, the Lagrangian approximation for impact and fragmentation problems can breakdown [26]. Guan et al. [26] addressed this with a semi-Lagrangian form of the RK approximation, where the nodes follow the material points (as in a Lagrangian discretization), but the kernel support measure is defined in the current configuration, $\phi_a(\mathbf{x} - \mathbf{x}(\mathbf{X}_I, t))$. The semi-Lagrangian form of the RK shape function is [26].

$$\Psi_I(\mathbf{x}) = \mathbf{H}^T(\mathbf{x} - \mathbf{x}(\mathbf{X}_I, t)) \mathbf{b}(\mathbf{x}) \phi_a(\mathbf{x} - \mathbf{x}(\mathbf{X}_I, t)) \quad (8)$$

An example of the Lagrangian and semi-Lagrangian kernel supports is shown in Fig. 1. The initial configuration in Fig. 1a undergoes a deformation, where the nodes follow the material points. In Fig. 1b, the Lagrangian kernel description causes the support to deform with the material, so that the set of neighbors contained in the kernel of node I remains the same before and after deformation. Alternatively, the semi-Lagrangian kernel, shown in Fig. 1c, is defined in the current configuration so that the kernel support is independent of the deformation. An important consequence of the semi-Lagrangian kernel support measure is that nodal neighbors are re-associated during deformation, which is key to the kernel contact algorithm discussed later.

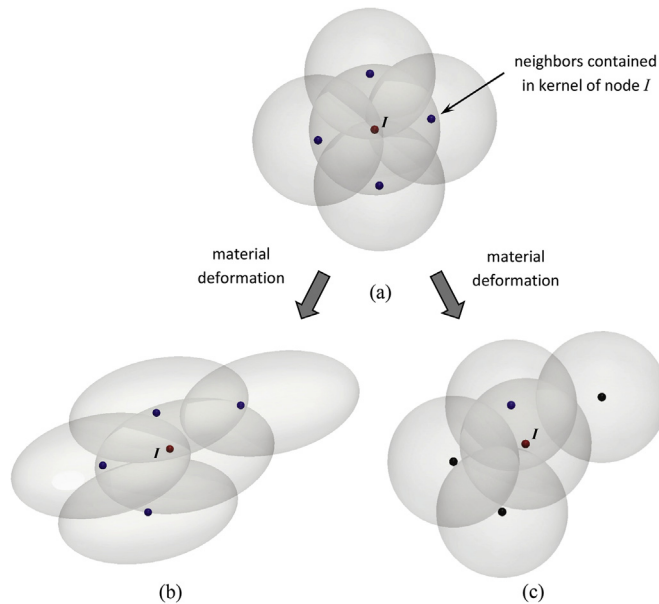


Fig. 1. Kernel support measure, a) initial configuration, b) Lagrangian kernel description, and c) semi-Lagrangian kernel description.

2.2. Stabilized nodal integration

Because of the lack of a conforming element topology in meshfree methods, special attention is required for numerical integration. Gauss integration can be used, but requires a background grid with associated high computational cost or large integration error due to lack of correspondence between the meshfree kernel support and integration subdomains [37]. Techniques for direct nodal integration are an attractive alternative as long as stability is appropriately addressed [31,32,38–40]. Consider the Galerkin weak form of the equation of motion

$$\int_{\Omega} \rho \mathbf{w}^h \cdot \ddot{\mathbf{u}}^h d\Omega + \int_{\Omega} \boldsymbol{\varepsilon}(\mathbf{w}^h) : \boldsymbol{\sigma}(\boldsymbol{\varepsilon}(\mathbf{u}^h)) d\Omega - \int_{\Omega} \mathbf{w}^h \cdot \mathbf{b} d\Omega - \int_{\Gamma^h} \mathbf{w}^h \cdot \mathbf{t} d\Gamma = 0 \quad (9)$$

where ρ is density, \mathbf{w}^h and \mathbf{u}^h are test and trial functions, $\boldsymbol{\varepsilon}$ is strain, $\boldsymbol{\sigma}$ is stress, Γ^h is the natural boundary, and \mathbf{b} and \mathbf{t} are body forces and surface tractions, respectively. Chen et al. [31,32] introduced a stabilized conforming nodal integration (SCNI) where gradients are approximated through a gradient smoothing operator

$$\bar{\boldsymbol{\varepsilon}}_I(\mathbf{u}^h) = (1/V_I) \int_{\partial\Omega_I} (1/2) (\mathbf{u}^h \otimes \mathbf{n} + \mathbf{n} \otimes \mathbf{u}^h) d\Gamma \quad (10)$$

where $\partial\Omega_I$ is the boundary of an integration sub-domain Ω_I (reference Fig. 2) corresponding to the I^{th} node, \mathbf{n} is the outward normal to the cell boundary, V_I is the strain smoothing cell volume, and $\bar{\boldsymbol{\varepsilon}}_I$ is the smoothed nodal strain. When this strain approximation is introduced to a direct nodal integration of Eq. (9), spurious zero energy modes are avoided, the linear patch test is satisfied, and computational efficiency is achieved since state and field variables are carried at the nodes [31]. SCNI is constructed on a conforming integration cell topology as shown in Fig. 2a, and is well suited for large distortion problems such as metal forming or rubber material deformation. However, the topologic structure in SCNI is difficult to maintain in the presence of material fragmentation, which is typical during concrete penetration. Accordingly, an alternative form, known as stabilized non-conforming nodal integration (SNNI), was also developed [32]. SNNI is constructed similarly to SCNI, but the conforming requirement on the smoothing cells is relaxed. A simple strain smoothing cell structure that is centered on the nodal material coordinate can be used (reference Fig. 2b), which provides an effective and efficient integration approach for problems involving material separation. A correction of SNNI to achieve optimal convergence has recently been proposed based on a variational consistency [41].

For these nodal integration techniques, under certain conditions spurious non-zero energy modes can still be activated due to loss of coercivity [33,42]. To correct for this condition, stabilization is introduced so that numerical integration of the internal force vector takes the form

$$\int_{\Omega} \boldsymbol{\varepsilon}(\mathbf{w}^h) : \boldsymbol{\sigma}(\boldsymbol{\varepsilon}(\mathbf{u}^h)) d\Omega = \sum_{I=1}^{np} \bar{\boldsymbol{\varepsilon}}_I(\mathbf{w}^h) : \boldsymbol{\sigma}(\bar{\boldsymbol{\varepsilon}}_I(\mathbf{u}^h)) V_I + \sum_{I=1}^{np} \sum_{J=1}^K \alpha \left[(\bar{\boldsymbol{\varepsilon}}_I(\mathbf{w}^h) - \boldsymbol{\varepsilon}_J(\mathbf{w}^h)) : \tilde{\mathbf{C}} : (\bar{\boldsymbol{\varepsilon}}_I(\mathbf{u}^h) - \boldsymbol{\varepsilon}_J(\mathbf{u}^h)) V_J \right] \quad (11)$$

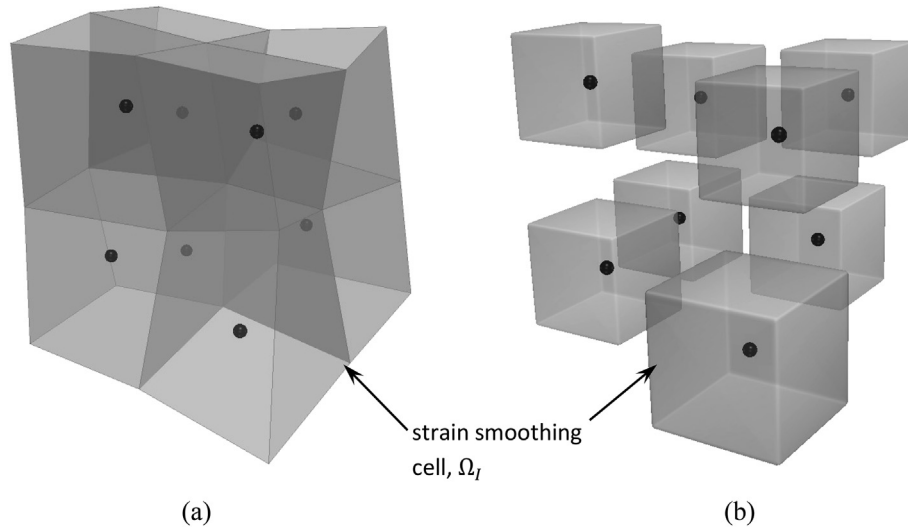


Fig. 2. Integration cell topology, a) SCNI conforming strain smoothing cells, b) SNNI non-conforming strain smoothing cells.

where $\hat{\mathbf{C}}$ is the consistent tangent modulus and α is a stabilization parameter ranging from 0 to 1 [42]. On the right hand side of Eq. (11), the first term is the standard internal force vector integration obtained by SCNI or SNNI. To provide the stabilization necessary to recover coercivity, the I^{th} integration cell is divided into K subdomains, and the second term in Eq. (11) is summed over these subdomains. The term ϵ_j is the strain computed at the subdomain centroid; the subdomain volume is V_j . Meshfree integration enriched with this additional stabilization is referred to as modified SCNI (M-SCNI) and modified SNNI (M-SNNI) [42].

2.3. Kernel contact algorithm

Multi-body contact is an essential aspect of impact and penetration problems, where the contact surfaces between penetrator and target evolve during the penetration process. Debris fields due to fragmentation are also typical and create an additional set of evolutionary contact conditions; this is especially true for brittle materials like concrete and can be particularly important when considering the effects of secondary debris on behind-target objects. In general, these contact conditions cannot be defined *a priori*, so it is important that methods for computational penetration mechanics be equipped to model them in a natural way. There are three important issues to be addressed, which are identification of the contact condition, enforcement of the impenetration constraint, and description of the contact forces between the bodies. These define the essential kinematic and kinetic constraints for the contact-impact problem [43].

Traditional contact algorithms generally involve the *a priori* definition of contact surfaces (master and slave surfaces) and rely on penalty or Lagrange multiplier techniques to enforce kinematic constraints [44–49]; other algorithms towards efficiency in contact constraint enforcement have also been developed, e.g. Refs. [50,51]. Because of the ease in re-association of nodal neighbors in the meshfree framework, methods like RKPM provide new opportunities to naturally model evolutionary contact conditions. Guan et al. [26] and Chi et al. [34] utilized the update of nodal interactions that results from the semi-Lagrangian RK approximation to automatically detect the contact of different bodies and naturally enforce the impenetration condition. This technique is referred to as a kernel contact algorithm and is used in this application for concrete penetration. The semi-Lagrangian kernel travels with the

same parent node during deformation, but its spatial measure is defined in the current configuration where the nodal neighbors evolve (reference Fig. 1); this provides the reference of contact conditions. The implication for contact detection is that as a body (Body A in Fig. 3) comes into contact with another (Body B in Fig. 3), the semi-Lagrangian kernel naturally detects the contact condition as the nodes from one body pass into the kernel support of a node in the other. Furthermore, the interaction forces between the bodies are naturally induced due to the overlapping kernels associated with nodes on Bodies A and B. This leads to an impenetration condition without additional treatment. The internal force, \mathbf{f}_I , at node I induced by the neighboring contacting nodes is [26,34].

$$\mathbf{f}_I = \sum_{j \in N_I^c} \bar{\mathbf{B}}_I^T(\mathbf{x}_j) \sigma_c(\mathbf{x}_j) V_j \quad (12)$$

where $\bar{\mathbf{B}}_I^T(\mathbf{x}_j)$ is the smoothed gradient from SCNI or SNNI, $\sigma_c(\mathbf{x}_j)$ is the contact stress, V_j is the nodal volume, $N_I^c = \{j | \phi_a(\mathbf{x}_I - \mathbf{x}_j) \neq 0, \mathbf{x}_j \in G_I \text{ or } G_I^*\}$, G_I is the set of all nodes in the body containing \mathbf{x}_I , $G_I^* = \{j | \mathbf{x}_j \notin G_I, \hat{\mathbf{n}} \cdot \sigma_c(\mathbf{x}_j) \cdot \hat{\mathbf{n}} < 0\}$, and $\hat{\mathbf{n}}$ is the unit normal vector to the contact surface. The condition $\hat{\mathbf{n}} \cdot \sigma_c(\mathbf{x}_j) \cdot \hat{\mathbf{n}} < 0$ indicates compression and ensures that contact forces are developed only when the surfaces are in a state of compressive contact. The contact stress, $\sigma_c(\mathbf{x}_j)$, is determined according to a Coulomb-type friction law.

Contact forces between the bodies are defined according to a friction-like elastic-plastic material law applied between the contact surfaces [26,34]. The behavior is assumed to follow similar to a plasticity law, where the yield function $f(\boldsymbol{\tau})$ and Karush–Kuhn–Tucker conditions are [34].

$$f(\boldsymbol{\tau}) = \|\boldsymbol{\tau}\| + \mu_f \hat{\sigma}_{11} \leq 0 \quad (13)$$

$$\dot{\boldsymbol{\epsilon}} = \gamma(\partial f(\boldsymbol{\tau}) / \partial \boldsymbol{\tau}) \quad (14)$$

$$\gamma \geq 0 \quad (15)$$

$$\gamma f(\boldsymbol{\tau}) = 0 \quad (16)$$

The yield function in Eq. (13) describes a stick-slip condition that follows similar to the Coulomb friction law, where $\boldsymbol{\tau} = [\hat{\sigma}_{12} \ \hat{\sigma}_{13}]$ is the tangential traction at the contact surface defined in a local

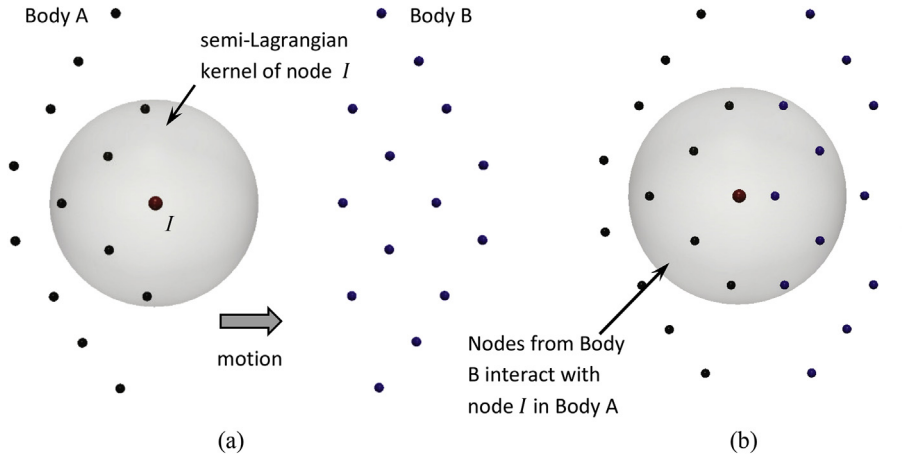


Fig. 3. Natural kernel contact detection, a) approaching bodies before contact, b) nodal interaction via semi-Lagrangian kernel after contact.

coordinate system, $\hat{\sigma}_{11}$ is the local compressive traction, μ_f is the coefficient of friction, and the local coordinate system is defined according to the contact surface outward normal. In Eq. (14)–(16) $\dot{\epsilon}$ is the tangential strain rate that describes the dynamic slip between the bodies and γ is the consistency parameter. Details of implementation of the natural contact algorithm which introduces the friction law in the form of an equivalent plasticity model can be found in Ref. [34].

Calculation of the contact forces requires a determination of the outward normal at the interface, which is not readily available in a meshfree framework where there is no element or cell topology to define the surface. Chi et al. [34] and Chen et al. [52] developed an algorithm that utilizes the level set method [53] to approximate the contact surface location and as a consequence define the surface outward normal. This approach utilizes the zero level set of a function, $\zeta(\mathbf{x})$, defined according to the semi-Lagrangian shape function

$$\zeta(\mathbf{x}) = \sum_{I \in N^A \cup N^B} \Psi_I(\mathbf{x}) C_I \quad (17)$$

where N^A represents the group of nodes in Body A (N^B is defined similarly), $\Psi_I(\mathbf{x})$ is the semi-Lagrangian shape function from Eq. (8), and C_I is a function defined as

$$C_I = \begin{cases} 1 & I \in N^A \\ -1 & I \in N^B \end{cases} \quad (18)$$

The contact surface is defined as the locations where $\zeta(\mathbf{x}) = 0$, which are obtained by numerical techniques [34,52]. As a consequence, the outward normal is approximated by

$$\hat{\mathbf{n}} = -\nabla \zeta(\mathbf{x}) / \|\nabla \zeta(\mathbf{x})\| \quad (19)$$

which is also numerically obtained [34,52].

2.4. Multi-scale concrete constitutive model

Many of the challenges in concrete penetration modeling are the result of shortcomings in the constitutive description. Various forms of phenomenological models are commonly used, but most often they lack a rigorous description of the fundamental response mechanisms. This is particularly true for the process of concrete damage, which is dominated by microstructure fracture. In order to work towards a more fundamental description of concrete failure, a multi-scale enhancement of the Advanced Fundamental Concrete

(AFC) model [54] was used to model the concrete targets in this study. The AFC model, developed by the U.S. Army Engineer Research and Development Center (ERDC), is a three-invariant plasticity model that includes hydrostatic crushing, material yielding, plastic flow, and damage effects. The damage function was enhanced through a multi-scale calculation [25], where microstructure fracture was explicitly modeled in a microcell, and free energy equivalence was used to derive a corresponding damage law for the continuum. This resulting damage law, known as a microcrack-informed damage model (MIDM), was embedded into the AFC model.

The experiments analyzed in this work used a concrete known as WES5000 that was developed by ERDC; an AFC material fit was developed by Adley et al. [54] and was used in this study. One of the key behaviors described by the AFC model is concrete's nonlinear response under hydrostatic compression, which is important when considering the large pressures generated in the impact region. As shown in Fig. 4, the hydrostatic behavior is assumed to consist of three response modes that describe the transition from initial elastic compression to a fully crushed and compacted material. The first response mode is the low-pressure elastic portion, where pressure, P and volumetric strain, μ , are related through the material bulk modulus, K_{bulk} . This elastic response extends to an experimentally determined initial crushing pressure (approximately 55 MPa for WES5000), which is defined in the model by two constants, C_6 and C_7 , that are the initial crushing pressure and initial crushing volumetric strain, respectively.

$$P = K_{bulk} \mu \quad \mu \leq C_7 \quad (20)$$

The second response mode is nonlinear crushing given by

$$P = K_1 \mu + K_2 \mu^2 + K_3 \mu^3 \quad (21)$$

where K_1 , K_2 , and K_3 are material constants. The nonlinear region extends to a point where the material is assumed to be fully crushed and the internal voids are collapsed to the maximum extent possible. At the end of nonlinear crushing the material is assumed to reach a so-called “locked state,” where the crushed particles are locked together and resistance to any further volumetric compression increases significantly. In the model, locking occurs at the point defined by a locking modulus and locking strain, C_8 and C_9 respectively, beyond which, the response is assumed to behave linearly according to the locking bulk modulus. Upon unloading in the linear locking region, the response follows the same locking modulus.

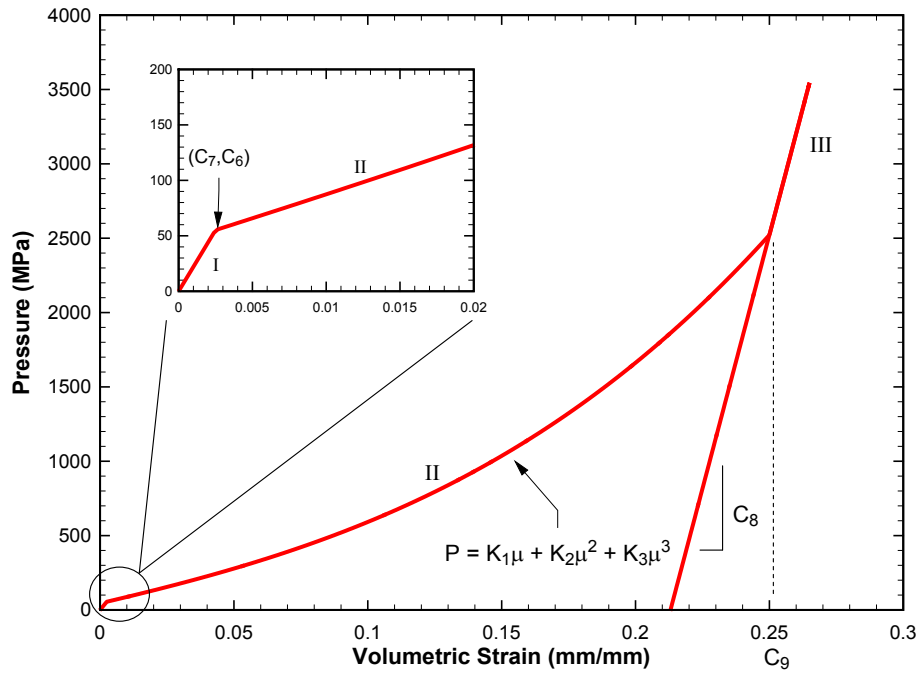


Fig. 4. The AFC hydrostatic fit for WES5000 concrete.

The rate-dependent shear failure surface in the AFC model is defined according to two functions, one for compression and one for tension. The compression failure surface is

$$S_Y^{comp} = (C_1 - (C_2 + (C_1 - C_2)d)e^{A_n I_1} - C_4 I_1)(1 + C_3 \ln(\dot{\epsilon}_n)), \quad (22)$$

where C_1 , C_2 , C_3 , C_4 , and A_n are material constants and d , I_1 , and $\dot{\epsilon}_n$ are damage parameter, first stress invariant, and a normalized strain-rate, respectively. Fig. 5 shows the compression failure surface for loading at both a quasistatic (0.001 s^{-1}) strain rate and a strain rate of 100 s^{-1} ; the model's rate dependence is observed. The tensile failure surface is defined by

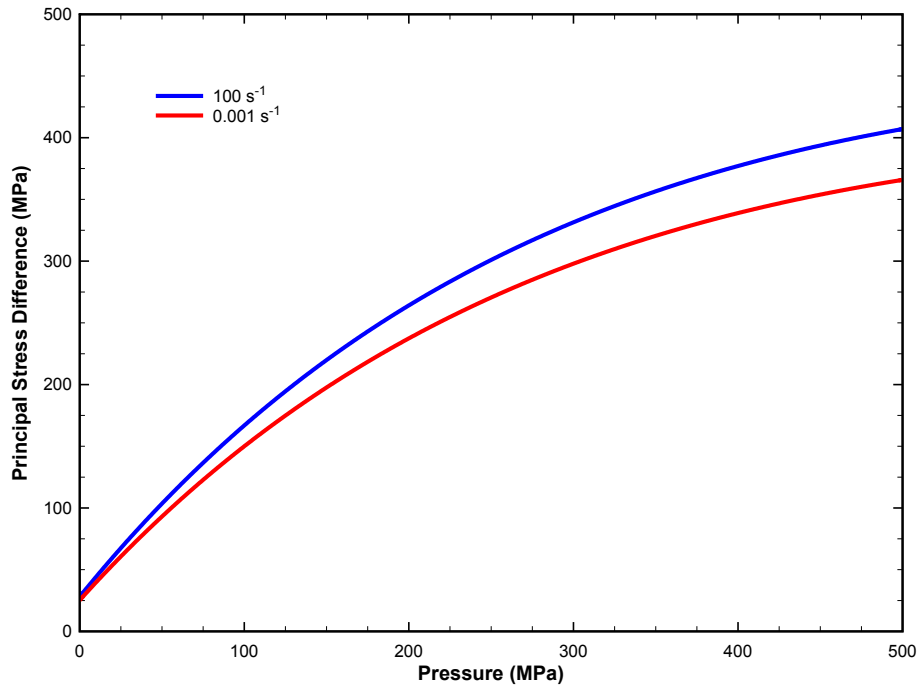


Fig. 5. AFC rate-dependent failure surface for WES5000. Two strain rates given to show the variation in strain rate response.

$$S_Y^{tens} = (C_1 - (C_2 + (C_1 - C_2)d))(1 + C_3 \ln(\dot{\epsilon}_n))(T_{max} - I_1)/T_{max}, \quad (23)$$

where T_{max} is the maximum allowed pressure in tension and d is the same damage parameter as used in Eq. (22). The AFC model also considers a modification of the failure surface for behavior in extension. The extension failure surface is determined by using the third stress invariant to calculate the Lode angle using a Willam–Warnke Lode function [55] which gives a reduction factor that is multiplied by Eq. (22). A final constant in the failure surface definition is C_5 , which limits the failure surface to a maximum allowable principal stress difference.

According to Eq. (22) and Eq. (23), tensile and compression failure in the AFC model are described according to a single damage parameter, d , that is defined as

$$d = \sum \left(\frac{\Delta \epsilon_p}{-I_1 D_1} + \frac{\Delta \mu_p}{1.5 C_9} \right) \quad d = \min(d, 1.0) \quad (24)$$

where D_1 and C_9 are material constants, and $\Delta \epsilon_p$ and $\Delta \mu_p$ are the increments in effective deviatoric plastic strain and plastic volumetric strain, respectively. A shortcoming of this description is that the damage evolution is purely phenomenological according to these plastic strains. Microstructure failure mechanisms, such as microcracking, are not accounted for in the model, although they provide a more accurate description of the material damage.

$$S_Y^{tens} = (C_1 - (C_2 + (C_1 - C_2)d))(1 + C_3 \ln(\dot{\epsilon}_n))(T_{max}(1 - d_t) - I_1)/(T_{max}(1 - d_t)) \quad (30)$$

Therefore, in order to improve the description of material failure a bi-scalar damage model was introduced, where shear damage was calculated using Eq. (24) and tensile damage was calculated using the MIDM. The tensile damage portion of the model was chosen for enhancement because of the significant impact that tensile failure can have during the penetration process of brittle materials. This bi-scalar damage form of the AFC model was originally proposed by Roth et al. [56].

The essential idea of the MIDM is to relate continuum damage to microstructure failure via energy-based bridging between scales [25]. With reference to Fig. 6, a representative microcell with domain Ω_y is assumed to contain microcracks with crack surfaces Γ_c and cohesive traction, \mathbf{h} (assuming a cohesive crack law). Failure of the microcell due to crack propagation is modeled according to the fracture mechanics, and the Helmholtz free energy (HFE) of the cracked microcell, Ψ^e , is obtained as

$$\Psi^e = \frac{1}{2} \boldsymbol{\sigma}^e : \boldsymbol{\epsilon}^e \quad (25)$$

where $\boldsymbol{\sigma}^e$ and $\boldsymbol{\epsilon}^e$ are the microcell stress and strain, respectively. The microcell HFE is related to the homogenized macroscale HFE, $\bar{\Psi}$, by

$$\bar{\Psi} = \frac{1}{V_y} \left(\int_{\Omega_y} \Psi^e d\Omega + \frac{1}{2} \int_{\Gamma_c} \mathbf{u}^e \cdot \mathbf{h} d\Gamma \right) \quad (26)$$

where V_y is the microcell volume and \mathbf{u}^e is the microcell displacement field [25]. In Eq. (26), the free energy of the homogenized continuum is a function of the microcell stress and strain and is also

a function of the microcrack opening displacement, which is modeled explicitly in the microcell model.

To relate the microcell fracture to a two-scalar continuum damage model [57], consider

$$\bar{\Psi} = (1 - d^+) \Psi_0^+ + (1 - d^-) \Psi_0^- \quad (27)$$

where d^+ and d^- are the damage parameters for tension and shear, respectively, and the free energy terms are defined according to the signs of the eigenvalues in the principal stress space [25]. The term Ψ_0 is the free energy corresponding with the undamaged continuum. Considering the Clausius–Duhem inequality of thermodynamics and

$$\dot{\Psi}_0^\pm = Y^\pm \quad (28)$$

where Y^\pm are the damage energy release rates, the microscale-informed tensile damage is obtained using Eq. (27) and Eq. (28)

$$d^+ = 1 - \frac{\partial \bar{\Psi}}{\partial Y^+} \approx 1 - \frac{\Delta \bar{\Psi}}{\Delta Y^+} \quad (29)$$

which can be evaluated numerically [25]. Using this approach, a tensile damage versus homogenized continuum strain relationship was determined for use in the WES5000 AFC model, as shown in Fig. 7. Letting $d^+ \equiv d_t$, the AFC tensile failure surface is modified as

so that the failure function is enriched with the microscale-driven behavior. Fig. 8 shows a comparison of the original AFC model tensile behavior with that of the AFC model using the MIDM enhancement. The original AFC model tensile behavior has a sharp discontinuity with no ability to capture material softening, which is a major shortcoming for simulations where tensile failure is a dominant response mode (as in concrete slab perforation). In contrast, the MIDM-enhanced model provides a more realistic softening branch that is guided by the microstructure conditions. The AFC model constants for the WES5000 material are listed in Table 1.

2.5. Penetrator and cylinder material model

For modeling the metals in this study, a simple J2 plasticity model with isotropic hardening was used. The material model constants are shown in Table 2, where the 4340 steel is used for the penetrator in the concrete penetration models and the 1090 steel and aluminum 6061-T6 were used in the benchmark Taylor bar tests to verify the proposed RKPM formulation. For the Taylor bar tests, both the 1090 steel and aluminum 6061-T6 exhibit only a small amount of hardening. Consequently, the behavior is simplified to an elastic-perfectly plastic response using the yield strengths reported in Wilkins and Guinan [58].

3. Verification experiments

3.1. Taylor bar experiments

Taylor bar cylinder experiments [58] are commonly used tests to validate the performance of numerical methods for large

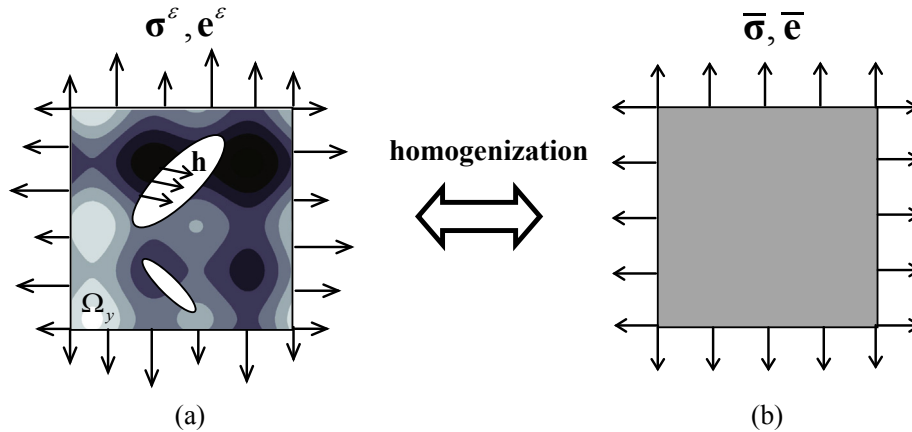


Fig. 6. Homogenization of microcell with fluctuating fields [51]; a) cracked microcell, b) homogenized continuum.

deformation solid dynamics. The Taylor bar test involves a short cylindrical rod impacting an anvil, i. e. near-rigid boundary, at sufficient velocity to induce large plastic flow in the contact region of the rod. Plastic strains may reach 200% or more, so that the test is an excellent measure of the ability to model large material deformations. Because of the relatively straightforward nature of the experiment and the deformation mode in the rod, the Taylor bar tests are widely used for method validation. For the RK impact and penetration formulation studied here, the Taylor bar experiment provides the opportunity to assess performance of the RKPM formulation with SNNI nodal integration and stabilization techniques in the presence of a large distortion problem. Furthermore, because the experiment is conducted by impacting the cylinder against the rigid anvil, it also provides the opportunity to test performance of the kernel contact algorithm. Validation of the formulation performance against these reasonably controlled experiments is used here as the basis for extension to the more complicated problems of large caliber concrete penetration, which

is the primary application of interest. For these Taylor bar simulations, the experiments from Wilkins and Guinan [58] were used to guide the numerical simulations. Wilkins and Guinan [58] performed a number of Taylor bar tests for different metallic materials including 1090 steel, aluminum 6061-T6, and many others. The setup of these tests is shown in Fig. 9. For the numerical simulations, the experiments with 1090 steel and aluminum 6061-T6 at velocities of 361 m/s and 373 m/s were selected. For both experiments, the initial length of the Taylor bar was 23.47 mm and the diameter was 7.62 mm. Both the bar and the rigid anvil were modeled to assess the deformation in the bar and also provide a measure of the contact algorithm performance.

3.2. SAP perforation experiments

The concrete perforation experiments by Cargile [59] were used in this study to assess performance of the RKPM impact and penetration formulation in the presence of complex penetration

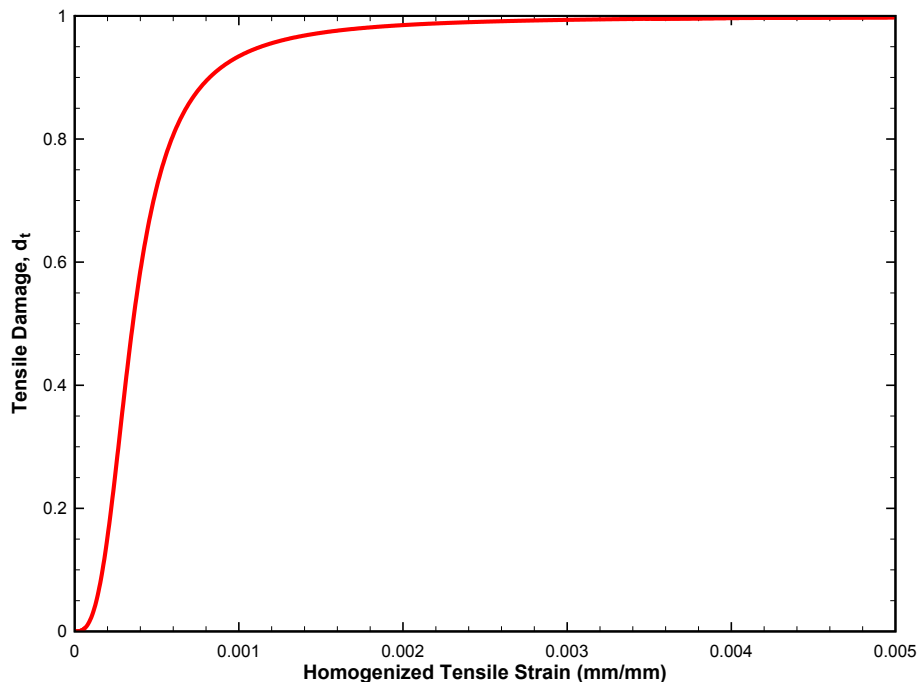


Fig. 7. Microcrack-informed tensile damage evolution function used for WES5000.

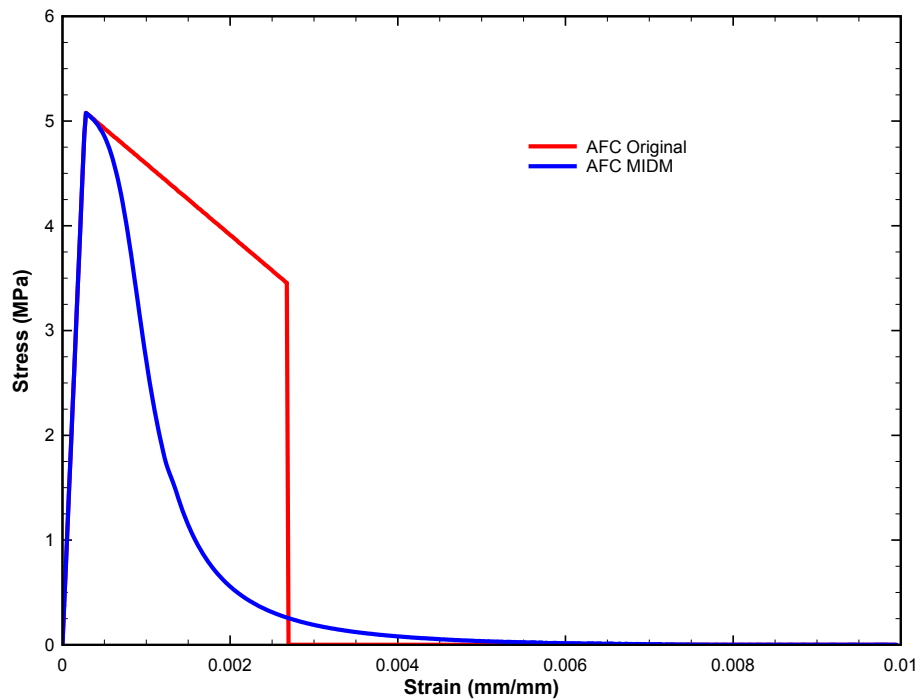


Fig. 8. Comparison of original AFC tension response to the AFC MIDM tension response.

processes. The experiments consisted of cylindrical unreinforced concrete (WES5000) slabs with a nominal unconfined compressive strength of 38.2 MPa. Further details of the WES5000 concrete targets can be found in Cargile [59]. The concrete slabs had a diameter of 1.52 m with thicknesses of 127 mm, 216 mm, and 257 mm. The three different thicknesses were selected to challenge the numerical simulation by providing three distinct target

response behaviors as described by Cargile [59]. The first thickness, 127 mm, is a thin slab that offers minimal resistance to the projectile, so that velocity reduction is largely governed by momentum exchange between projectile and target. The second thickness, 216 mm, is a moderate thickness slab so that the target strength and projectile-target interaction have a more significant effect. The

Table 1
AFC model constants for WES5000.

Parameter	Value
Density (kg/m^3)	2267
Shear modulus (MPa)	6892.7
C_1 (MPa) – Failure surface constant	501.05
C_2 (MPa) – Failure surface constant	476.3
C_3 – Failure surface constant	0.01
C_4 – Failure Surface Constant	0.1
C_5 (MPa) – Failure surface constant	516.95
C_6 (MPa) – Pressure where crushing begins	55.14
C_7 – Volumetric strain at crushing	0.0025
C_8 (MPa) – Locking modulus	68,237
C_9 – Volumetric strain at locking	0.25
K_1 (MPa) – Hydrostatic compression constant	4248.3
K_2 (MPa) – Hydrostatic compression constant	6196.5
K_3 (MPa) – Hydrostatic compression constant	68,237
D_1 (MPa^{-1}) – Damage constant	0.0006
A_N (MPa^{-1}) – Failure surface constant	0.00324
T_{\max} (MPa) – Maximum allowable tensile pressure	2.47

Table 2
J2 plasticity model parameters for metals in this study.

Parameter	4340 Steel	1090 Steel	Al 6061-T6
Young's modulus (GPa)	205	205	78.6
Poisson's ratio	0.26	0.29	0.33
Yield stress (MPa)	1750	1200	420
Hardening modulus (MPa)	1000	0	0
Density (kg/m^3)	7860	7860	2700

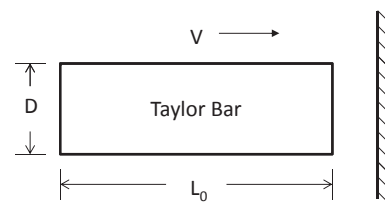


Fig. 9. Setup of Taylor bar cylinder test where L_0 is the initial length, D is the diameter, and V is the initial velocity.

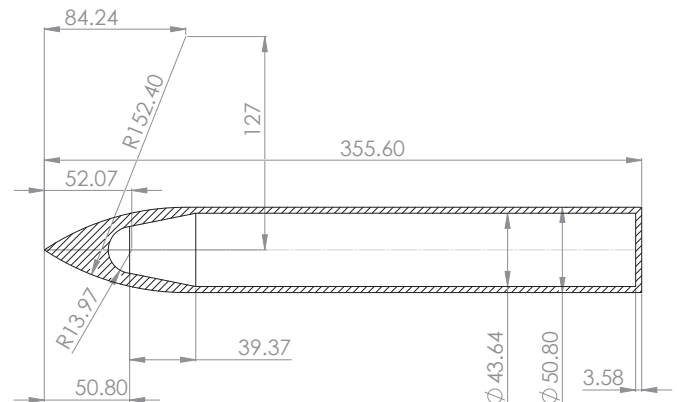


Fig. 10. Dimensions of SAP projectile. All dimensions are in millimeters.

last thickness, 254 mm, is a relatively thick slab that is approaching the perforation limit of the projectile at 313 m/s. In this case the projectile is nearly stopped by the slab, so that strength and interaction effects are of significant importance. The projectile used in the study was a semi-armor piercing (SAP) projectile illustrated in Fig. 10. The SAP projectile was launched from an 83-mm diameter gun at an approximate velocity of 313 m/s for all experiments. The projectile was composed of a heat treated 4340 steel casing and an inert filler (typically sand). Due to the large difference in strengths between the projectile and target, the projectile experienced little deformation.

As a consequence of the different types of observed target response modes, the simulations provide a good test of formulation performance across a range of conditions. The contact detection algorithm is exercised as a result of the evolving contact surfaces between the penetrator and target, where an accurate representation is crucial to accurately model the effects of penetrator–target interaction. Fracture and debris formation is also an important aspect of the target behavior, where the concrete damage localizes in two different brittle failure mechanisms. The first mechanism occurs in the immediate vicinity of the impact zone, where the concrete material is crushed and pushed out of the way of the penetrating projectile. Fracture and debris formation on the impact and exit faces is the typical result. The second failure mechanism is the formation of radial cracks that grow in the far-field regions away from the penetration zone. These types of deformations and failure mechanisms are challenging to capture in numerical models, and therefore provide good tests of this method's overall ability to capture dynamic, brittle material failure.

4. Numerical model

The RKPM impact and penetration formulation was implemented in NMAP [30]. NMAP is a parallel, three-dimensional, explicit RKPM-based code developed for the dynamic analysis of linear and nonlinear solid mechanics problems. The code implements Lagrangian and semi-Lagrangian RK approximations that are selectable by the user based on the problem being modeled. An updated Lagrangian framework is used to model geometric and material nonlinearity, and objective stress calculations are ensured by use of the Hughes–Winget algorithm for stress update [60]. Spatial integration is performed using either SCNI [31] or SNNI [33] and can be selected by the user based on the problem requirements. The stabilized integration techniques, M-SCNI and M-SNNI, based on Chen et al. [33] are also included as options. Time integration is performed using Newmark time integration, and the integration constants can be specified for desired accuracy. Multi-body contact is modeled using the kernel contact algorithm, where the normal and tangential contact forces are computed according to the Coulomb-type material law. The outward normal at the contact interface can be computed according to the directional vector between paired nodes or using the level set technique, both of which are available as user selectable options.

4.1. Taylor bar model

The Taylor bar model consisted of a cylinder with the dimensions discussed in section 3.1 fired at a rigid plate for the bar to impact. The cylinder was discretized with approximately 22,000 nodes. The semi-Lagrangian RK approximation was used along with the SNNI and M-SNNI techniques for weak form integration. The original and modified SNNI were used in order to compare stability of the integration techniques for this type of large deformation problem. The kernel contact algorithm with the level set-based outward normal calculation was used to model the contact

condition. A small amount of friction between the Taylor bar and the anvil was used in order to better capture the contact condition and its effect on the bar deformation. The J2 plasticity model was used to model the metals, with constants as shown in Table 2. Both the steel and aluminum experiments were modeled at their respective initial velocities and the simulations were allowed to run until the bar began to rebound from the rigid plate.

4.2. SAP perforation model

The SAP perforation model consisted of the SAP projectile fired at the WES5000 concrete targets with the specified thicknesses. Deformation of the projectile fill and its interaction with the casing was not a focus of this study, so the projectile was simplified by not explicitly including the fill shown in Fig. 10. Instead, the fill mass was incorporated into the steel casing by increasing the density of the steel so that the projectile had the correct overall mass. Because the experimentally-observed projectile deformation is very small, this was not expected to have an impact on results. With the additional mass incorporated into the steel casing, the density of the casing was increased from 7860 kg/m³ shown in Table 2 to 11,248 kg/m³, which preserved the overall projectile mass.

The three different WES5000 target thicknesses of 127 mm, 216 mm, and 254 mm, were discretized with approximately 47,000 nodes, 67,000 nodes, and 77,000 nodes, respectively. Additionally, a higher refinement model of approximately 152,000 nodes was included in the 127 mm case in order to demonstrate the effects of mesh refinement. This resulted in a low resolution model of 8 nodes through the 127 mm target thickness and 13 nodes through the higher resolution thickness. The semi-Lagrangian RK approximation was used with the M-SNNI integration due to the large amount of fracturing present in the perforation event. The kernel contact algorithm was also used in conjunction with the level set outward normal detection to model the multi-body contact. The SAP projectile used in all the simulations was discretized with 4825 nodes, and the initial velocity was 313 m/s as described in section 3.2. Each simulation ran until the SAP projectile exited the back side of the slab, and then the simulation was stopped.

5. Results and discussion

5.1. Taylor bar

Two sets of Taylor bar simulations were performed. In the first set the aluminum Taylor bar was modeled, where SNNI and M-SNNI results were compared to assess their performance in the presence

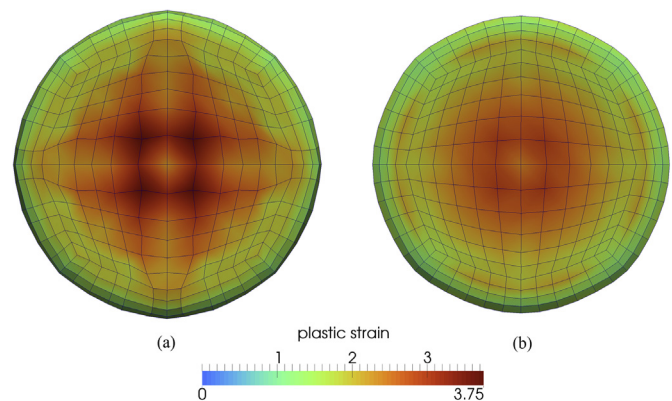


Fig. 11. Plastic strain contours for a) SNNI and b) M-SNNI simulations of the aluminum Taylor bar test.

of large plastic deformations. Fig. 11 shows the comparison between SNNI and M-SNNI for the bottom of the deformed bar. The particles from the NMAP simulation were post-processed to superimpose an element structure on the nodal discretization in order to highlight the differences in the computed deformations. Fig. 11a clearly shows the emergence of the spurious non-zero energy modes in the SNNI simulation, which manifest themselves as hourglass-like deformation modes throughout the bar. The SNNI results also showed localized regions of higher plastic strain, with a maximum magnitude of 3.75. In contrast, the deformation and plastic strain in the M-SNNI results were much more uniform, with a maximum plastic strain value of 2.98. Although the experimental strain values are not known, based on the computed deformations the M-SNNI results are expected to be more accurate, so that the SNNI maximum plastic strain was an approximate 25 percent overshoot. A difference in the deformed shapes at the edge of the bar was also observed. In the SNNI case a substantial lip exists on the outer edge that is not present in the experimentally-observed deformation. The M-SNNI method provided a more uniform and realistic deformation at the bar's edge. Finally, the computed diameters of the deformed bars differed, with a final bottom diameter for the SNNI simulation of 16.26 mm and a final M-SNNI diameter of 15.68 mm. Based on these results, M-SNNI was determined to be more accurate and was therefore used for all other simulations herein.

The second set of Taylor bar simulations modeled the aluminum and steel cylinder impacts, with results shown in Fig. 12. In both of these simulations only the M-SNNI feature was used so that the spurious SNNI response modes were avoided. The kernel contact algorithm was used, and the results showed that it accurately captured the contact conditions between the bar and rigid surface. The two experiments showed similar results for final length, even though the materials have different densities and strengths; this was accurately captured in the numerical results. Table 3 displays a comparison of the final length ratio for both the aluminum and steel bar tests. NMAP did an adequate job of matching the experimental results of both Taylor bar tests. The minimal difference between the experiment results and the NMAP simulations is attributed to the material models used, where a more robust model with more accurate plasticity and damage description may further close the gap between the experimental and the numerical results.

5.2. SAP perforation

The results of the three lower resolution SAP projectile simulations are shown in Fig. 13 at the point when the projectile exits

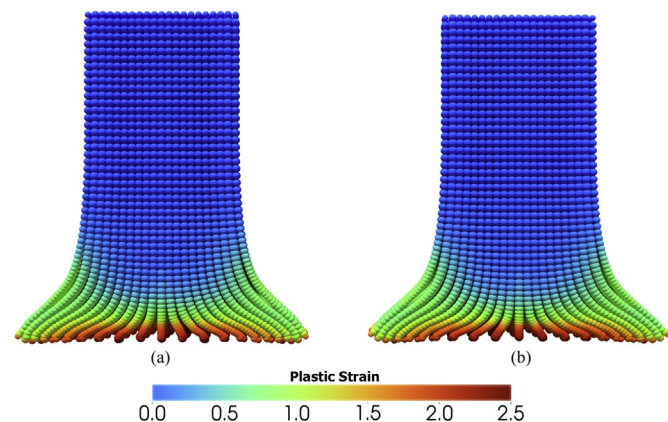


Fig. 12. Plastic strain contours for M-SNNI Taylor bar cylinders tests of a) aluminum and b) steel.

Table 3

Ratio of initial to final lengths for experimental and modeled Taylor bar cylinder tests.

	NMAP final length ratio	Experiment final length ratio
Aluminum	0.724	0.703
Steel	0.7285	0.696

each target. For the thinner target, the damage area is localized since the material fails quickly because of the proximity of the free back surface. The general trend from Fig. 13 is that, with increased target thickness, the model predicts a larger damaged area. This is consistent with the expected experimental damage patterns, because as target thickness increases, more of the projectile's energy is absorbed and produces larger damage zones. These observations validate the formulation's ability to model the penetration-induced damage for this type of problem. One feature that was missing from the lower resolution models was clear localization of radial cracks, where the higher resolution model of the 127 mm slab thickness displayed localization of radial cracks. Fig. 14 shows a comparison between the lower resolution model and the higher resolution model from the top and bottom of the concrete slab. Only the damage values between 0.15 and 1.0 are shown in order to show the dominant damage features of these two simulations. For an additional comparison of the 127 mm case, the velocity histories

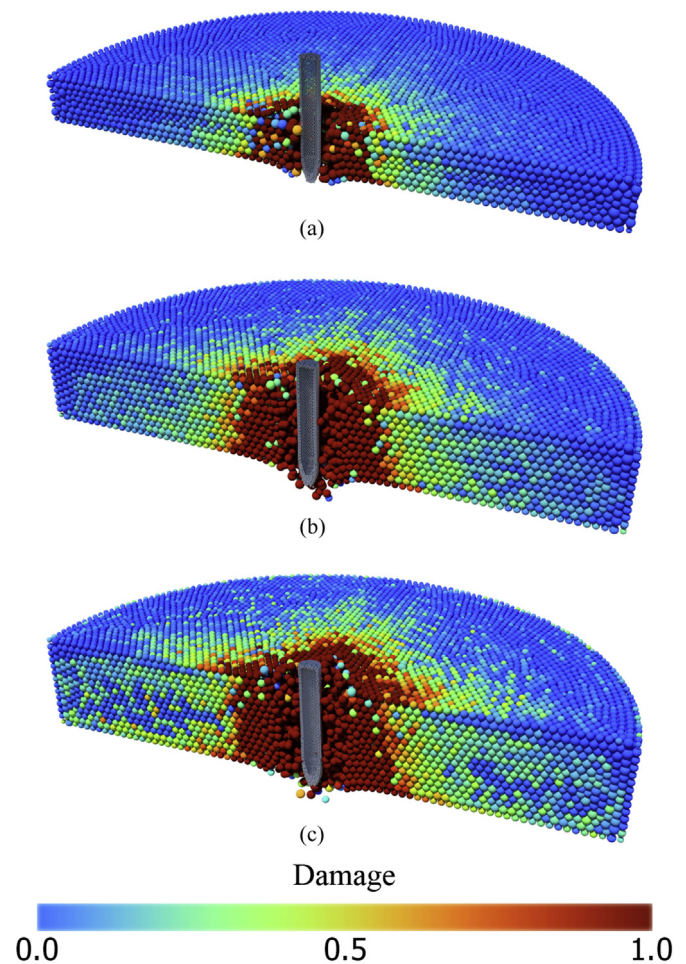


Fig. 13. Damage contours for SAP perforation low resolution models with thicknesses of a) 127 mm, b) 216 mm, and c) 254 mm. Note that some of the particles were removed for clarity.

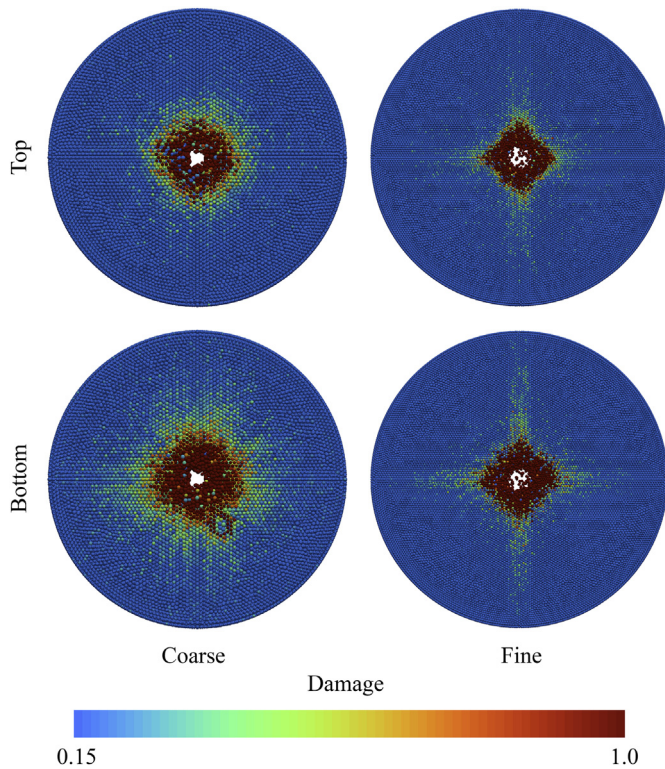


Fig. 14. Top and bottom face damage contours comparison for both the low resolution and high resolution model of the 127 mm case.

of the low and high resolution models are shown in Fig. 15 along with the experimental result. Fig. 15 also includes the 127 mm simulation data from the recent work of Sherburn et al. [61] which used a coupled Eulerian–Lagrangian approach to model the same

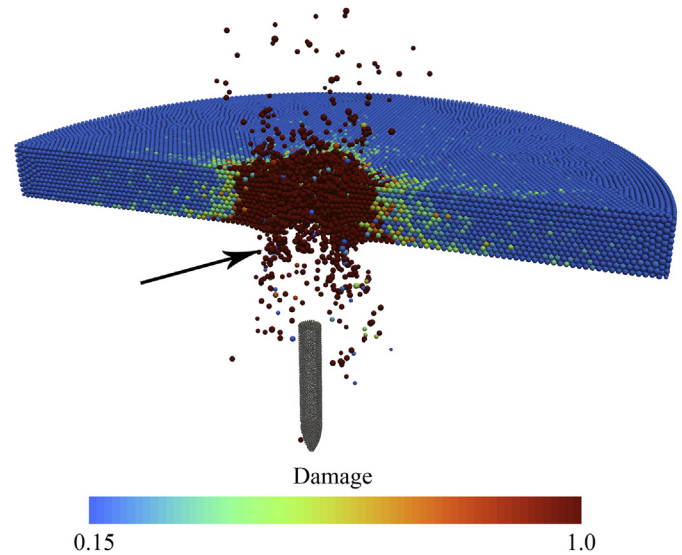


Fig. 16. Damage contours for 127 mm high resolution simulation with the debris field and ejecta shown. The included arrow points toward a cluster of nodes that represents a sizable piece of concrete that has broken off the slab's back face.

experiment. These results show that the predicted projectile exit velocity in the higher resolution model reasonably matches with the experimental and is higher than that from the coarser model, which is expected based on more accurate capture of the strain softening failure mechanism. An important strength of the mesh-free method is its ability to naturally capture the debris field off the slab back face and the ejecta off the front face that is generated as a penetrator impacts the target. Fig. 16 depicts an emerging debris field from the 127 mm high resolution model. From both the debris field and ejecta, larger pieces of concrete can be seen breaking off the target in the form of clusters of nodes. These represent blocks of

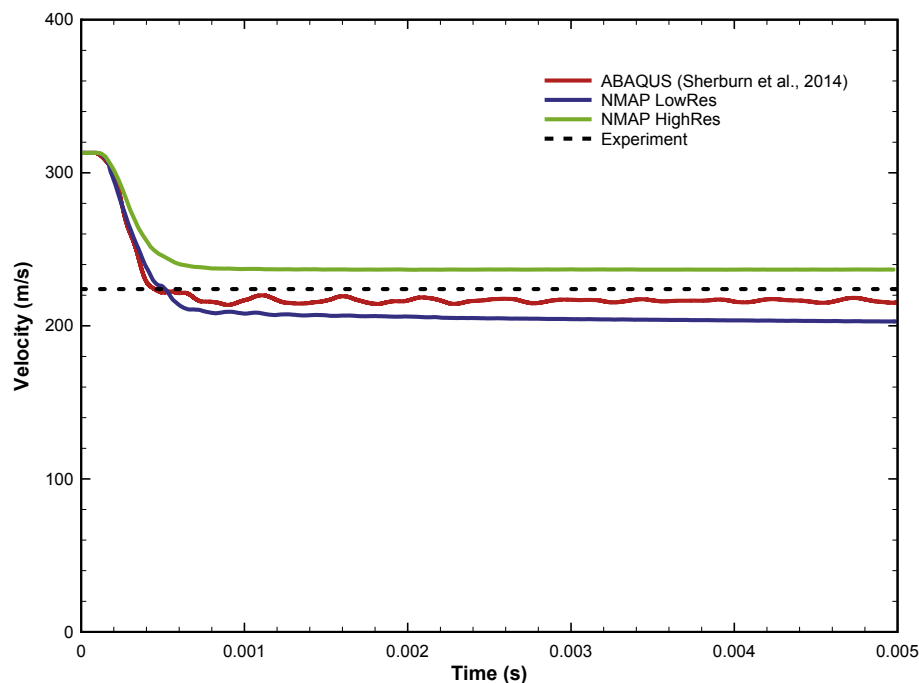


Fig. 15. Velocity time histories for the low and high resolution models compared to the experimental result. The analogous 127 mm simulation result from Sherburn et al. [61] is also included.

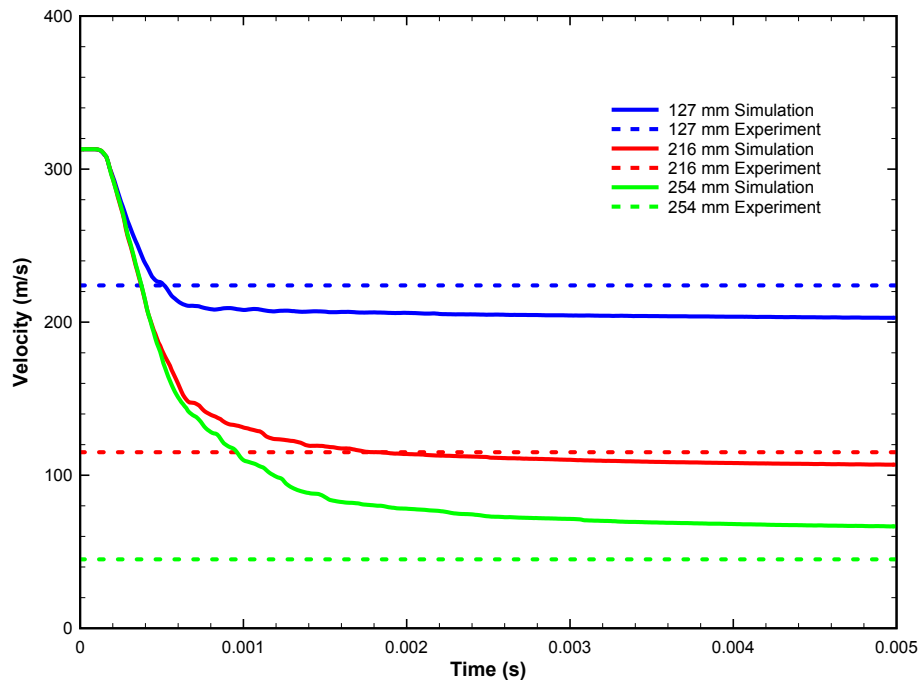


Fig. 17. Velocity time history of the SAP penetrator for the three different slab thicknesses.

material that are fractured off the main slab. The ability to accurately capture this aspect of target failure is important for these problem types, particularly when considering effects like behind-armor debris fields and their impact on secondary targets. This is not well captured in traditional Lagrangian methods where techniques like element erosion are required, nor in Eulerian methods where the fragmented material tends to be smeared. Another point of comparison between the low and high resolution model is the hole shape and the damage zone around the impact zone. As shown in Fig. 16 both resolutions have a similar hole size, with the higher resolution model having a slightly larger hole size. In terms of damage zone comparison the lower resolution model has a slightly larger damage zone than the higher resolution model. As expected, the SAP projectile experienced little deformation during the penetration event in all three thickness scenarios. Fig. 17 displays the SAP projectile's velocity-time history for each of the low resolution simulation and includes the respective experimental final velocity for trend comparisons. Over the thickness range, the NMAP simulations captured the trend of the experimental results reasonably well. A direct comparison of the experimental and NMAP low resolution simulation results is shown in Table 4. Considering change in velocity, the greatest variation between experimental and NMAP results came from the 254 mm thickness, which had a difference of 6.9%. Considering change in kinetic energy, the 127 mm NMAP simulation had the greatest difference of 8.1%. A final point of comparison between the experiments and the low resolution simulations is the impact and exit crater patterns computed after the projectile exited the targets, which are shown in Fig. 18. In all three cases the simulated impact craters matched the experimental results reasonably well, especially considering the heterogeneous nature of the concrete. There was somewhat greater deviation for the exit crater predictions. Achieving an exact match to the exit crater shape is difficult, and a further improved tensile damage evolution relationship may improve the match.

One of the difficulties of numerical simulation of concrete is its inherent stochastic nature. The experiments performed by Cargile [59] only included the results of a few tests for each thickness, but

these contained inherent variation due to the concrete's stochastic mechanical response. The simulations however are deterministic, and do not capture this effect. Concrete is a non-homogeneous material made up of aggregates of various sizes, cementitious paste, and air voids. Some microcracking will always be present as an artifact of the curing and drying processes. The MIDM helps bridge the scales by homogenization of the microcell problem to the macroscale simulation, but the variation that occurs in the material is not captured using the current form. Work towards the inclusion of stochastic material microstructure variation into the MIDM has been performed [62] and is considered for future implementation into the NMAP code.

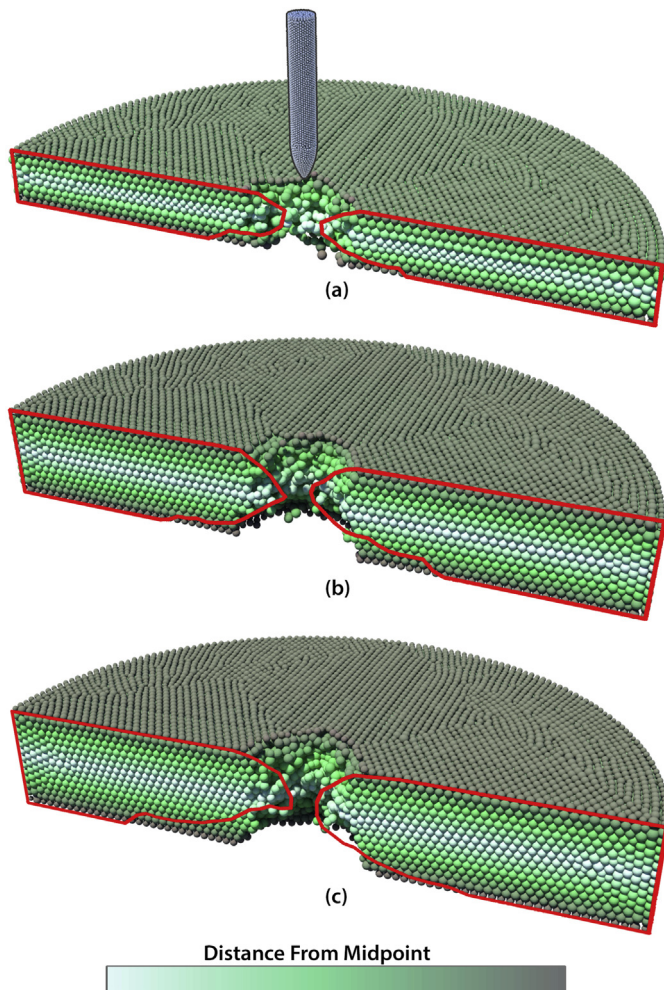
6. Conclusions

In this work an RKPM-based impact and penetration formulation was presented, which was implemented in the UCLA-UCSD and ERDC developed NMAP code. Several key features for mesh-free concrete penetration modeling were introduced, which included a robust technique for domain integration, natural kernel contact, and a multi-scale damage model to describe the concrete failure. The accuracy of this formulation was studied for large-caliber projectile penetration into concrete slabs, where mechanisms such as evolutionary contact and concrete fracture are critical elements to capture in the numerical model. To address the issue of meshfree domain integration in the presence of material fragmentation, SNNI was implemented into NMAP. This meshfree integration technique, which uses a simple integration cell topology that can easily move with separating materials, was first validated for a series of Taylor bar impact tests. Numerical experiments showed that the SNNI implementation in NMAP was able to accurately model the large deformations measured in the experiments. Furthermore, spurious non-zero energy modes that may appear in the numerical results can be suppressed by recovering coercivity with stabilization of the internal force vector integration. Based on these results, the stabilized meshfree integration method, known as M-SNNI, was concluded to also be an accurate and

Table 4

Comparison between SAP projectile experiments and NMAP simulations.

Thickness (mm)	Experimental exit velocity (m/s)	Experimental Δ velocity (%)	Experiment Δ KE (%)	Simulation exit velocity (m/s)	Simulation Δ velocity (%)	Simulation Δ KE (%)
127	224	28.4	48.8	205.4	34.4	56.9
216	115	63.3	86.5	107.6	65.6	88.1
254	45	85.6	97.9	66.6	78.7	95.4

**Fig. 18.** Comparison of experimental and low resolution simulated impact and exit crater profiles for thicknesses of a) 127 mm, b) 216 mm, and c) 254 mm.

effective integration method for meshfree concrete penetration modeling.

Another important element introduced to the NMAP code was natural kernel contact, which is enabled as a result of the semi-Lagrangian approximation. This approach is very effective for evolutionary contact problems like projectile penetration since it does not require an *a priori* definition of contact surfaces. Furthermore, considering that the semi-Lagrangian formulation is able to model material separation without the traditional concerns over mesh separation or entanglement, debris fields that might interact with secondary targets can be naturally captured. This is an important capability for modeling complex structures that is not readily achieved using conventional mesh-based methods. Using the NMAP code, the formulation was validated against three concrete perforation experiments with a constant projectile velocity and differing target thicknesses. Terminal ballistic conditions

varied strongly between the three experiments, with the projectile kinetic energy reduction ranging from 49 to 98 percent. The numerical results followed closely across this range of conditions, with an error of not more than 8 percent. The numerical results at the end of the simulation also reasonably matched the post-test crater patterns. This indicates that the multi-scale material damage model captured the fundamental failure mechanisms with reasonable accuracy, providing a strong foundation for further enhancement through more robust descriptions of the heterogeneous and stochastic microstructure properties.

Acknowledgments

Permission to publish was granted by the Director, Geotechnical and Structures Laboratory, U.S. Army Engineer Research and Development Center. Simulations were partly performed on the Department of Defense Super Computing Resource high performance computers. Financial support from the U.S. Army Engineer Research and Development Center (Contract No. W912HZ-07-C-0019) to UCLA and its subcontract to UC San Diego is greatly acknowledged.

References

- [1] Zukas JA, editor. *High velocity impact dynamics*. New York: John Wiley and Sons; 1990.
- [2] Bishop RF, Hill R, Mott NF. The theory of indentation and hardness. *Proc Phys Soc* 1945;57:147–59.
- [3] Kennedy RP. A review of procedures for the analysis and design of concrete structures to resist missile impact effects. *Nucl Eng Des* 1976;37:183–203.
- [4] Backman ME, Goldsmith W. The mechanics of penetration of projectiles into targets. *Int J Eng Sci* 1978;16:1–99.
- [5] Wilkins ML. Mechanics of penetration and perforation. *Int J Eng Sci* 1978;16:793–807.
- [6] Jonas GH, Zukas JA. Mechanics of penetration: analysis and experiment. *Int J Eng Sci* 1978;16:879–903.
- [7] Aptukov VN. Penetration: mechanical aspects and mathematical modeling (review). *Strength Mater* 1990;22(2):230–40.
- [8] Anderson Jr CA, Bodner SR. Ballistic impact: the status of analytical and numerical modeling. *Int J Impact Eng* 1988;7(1):9–35.
- [9] Ben-Dor G, Dubinsky A, Elperin T. Recent advances in analytical modeling of plate penetration dynamics – a review. *Appl Mech Rev* 2005;58:355–71.
- [10] Forrestal MJ, Luk VK. Dynamic spherical cavity expansion in a compressible elastic-plastic solid. *ASME J Appl Mech* 1988;55(2):275–9.
- [11] Luk VK, Forrestal MJ, Amos DE. Dynamic spherical cavity expansion of strain-hardening materials. *ASME J Appl Mech* 1991;58(1):1–6.
- [12] Forrestal MJ, Luk VK. Penetration into soil targets. *Int J Impact Eng* 1992;12(3):427–44.
- [13] Forrestal MJ, Tzou DY. A spherical cavity-expansion penetration model for concrete targets. *Int J Solids Struct* 1997;34(31–32):4127–46.
- [14] Littlefield DL, Anderson Jr CE, Partom Y, Bless SJ. The penetration of steel targets finite in radial extent. *Int J Impact Eng* 1997;19(1):49–62.
- [15] Sataphathy S. Dynamic spherical cavity expansion in brittle ceramics. *Int J Solids Struct* 2001;38(32–33):5833–45.
- [16] Sewell DA, Ong ACJ, Hallquist JO. Penetration calculation using an erosion algorithm in DYNA. In: Riegel J, Murphy MJ, editors. *Proceedings of the 12th international symposium on Ballistics*, vol. 3. San Antonio, TX: American Defense Preparedness Association; 1990. p. 208–17.
- [17] Johnson GR, Stryk RA. Eroding interface and improved tetrahedral element algorithms for high-velocity impact computations in three dimensions. *Int J Impact Eng* 1987;5:411–21.
- [18] Belytschko T, Lin A. A three-dimensional impact-penetration algorithm with erosion. *Int J Impact Eng* 1987;5:111–27.
- [19] Leveque RJ. *Finite difference methods for ordinary and partial differential equations: steady state and time-dependent problems*. Philadelphia: Society for Industrial and Applied Mathematics; 2007.

- [20] Leveque RJ. Finite volume methods for hyperbolic problems. New York: Cambridge University Press; 2002. p. 580.
- [21] Lee K, Moorthy S, Ghosh S. Multiple scale computational model for damage in composite materials. *Comput Methods Appl Mech Eng* 1999;172:175–201.
- [22] Fish J, Yu Q, Shek K. Computational damage mechanisms for composite materials based on mathematical homogenization. *Int J Numer Methods Eng* 1999;45:1657–79.
- [23] Dascalu C, Bilbie G, Agiasofitou EK. Damage and size effects in elastic solids: a homogenization method. *Int J Solids Struct* 2008;45:409–30.
- [24] Dascalu C. A two-scale damage model with material length. *Comptes Rendus Mec* 2009;337(9–10):645–52.
- [25] Ren X, Chen JS, Li J, Slawson TR, Roth MJ. Micro-cracks informed damage models for brittle solids. *Int J Solids Struct* 2011;48:1560–71.
- [26] Guan PC, Chi SW, Chen JS, Slawson TR, Roth MJ. Semi-Lagrangian reproducing kernel particle method for fragment-impact problems. *Int J Impact Eng* 2011;38:1633–47.
- [27] Chen JS, Wu Y, Guan P, Teng H, Gaidos J, Hofstetter K, et al. A Semi-Lagrangian reproducing kernel formulation for modeling earth moving operations. *Mech Mater* 2009;41:670–83.
- [28] Liu WK, Jun S, Zhang YF. Reproducing kernel particle methods. *Int J Numer Methods Fluids* 1995;20:1081–106.
- [29] Chen JS, Pan C, Wu CT, Liu WK. Reproducing kernel particle methods for large deformation analysis of nonlinear structures. *Comput Methods Appl Mech Eng* 1996;139:49–74.
- [30] Chi SW, Lee CH, Chen JS, Roth MJ, Slawson TR. User's manual for non-linear meshfree analysis program (NMAP), version 1.0. Technical Report ERDC/GSL TR-12–36. Vicksburg, MS: U.S. Army Engineer Research and Development Center; 2012. p. 86.
- [31] Chen JS, Wu CT, Yoon S, You Y. A stabilized conforming nodal integration for Galerkin meshfree methods. *Int J Numer Methods Eng* 2001;50:435–66.
- [32] Chen JS, Yoon S, Wu CT. Nonlinear version of stabilized conforming nodal integration for Galerkin meshfree methods. *Int J Numer Methods Eng* 2002;53:2587–615.
- [33] Chen JS, Hu W, Puso M, Wu Y, Zhang X. Strain smoothing for stabilization and regularization of Galerkin meshfree method. *Lect Notes Comput Sci Eng* 2006;57:57–76.
- [34] Chi SW, Lee CH, Chen JS, Guan PC. A level set enhanced natural kernel contact algorithm for impact and penetration modeling. *Int J Numer Methods Eng* 2014. <http://dx.doi.org/10.1002/nme.4728>.
- [35] Gingold RA, Monaghan JJ. Smooth particle hydrodynamics: theory and applications to non-spherical stars. *Mon Notices R Astronomical Soc* 1977;181:375–89.
- [36] Chen JS, Wang HP. New boundary condition treatments in meshfree computation of contact problems. *Comput Methods Appl Mech Eng* 2000;187:441–68.
- [37] Dolbow J, Belytschko T. Numerical integration of Galerkin weak form in meshfree methods. *Comput Mech* 1999;23:219–30.
- [38] Beissel S, Belytschko T. Nodal integration of the element-free Galerkin method. *Comput Methods Appl Mech Eng* 1996;139:49–74.
- [39] Randles PW, Libersky LD, Petschek AG. On neighbors, derivatives, and viscosity in particle codes. In: Wunderlich W, editor. *Proceedings of ECCM conference*; Munich, Germany; 1999.
- [40] Bonet J, Kulasegaram S. Correction and stabilization of smooth particle hydrodynamics methods with applications in metal forming simulation. *Int J Numer Methods Eng* 1999;47:1189–214.
- [41] Chen JS, Hillman M, Rüter M. An arbitrary order variationally consistent integration method for Galerkin meshfree methods. *Int J Numer Methods Eng* 2013;95:387–418.
- [42] Puso MA, Chen JS, Zywick E, Elmer W. Meshfree and finite element nodal integration methods. *Int J Numer Methods Eng* 2008;74:416–46.
- [43] Belytschko T, Liu WK, Moran B. Nonlinear finite elements for continua and structures. New York: John Wiley and Sons; 2000. p. 300.
- [44] Hallquist JO, Goudreau GL, Benson DJ. Sliding interfaces with contact-impact in large-scale Lagrangian computations. *Comput Methods Appl Mech Eng* 1985;51:107–37.
- [45] Carpenter NJ, Taylor RL, Katona MG. Lagrange constraints for transient finite element surface contact. *Int J Numer Methods Eng* 1991;32:103–28.
- [46] Belytschko T, Neal MO. Contact-impact by the pinball algorithm with penalty and Lagrangian methods. *Int J Numer Methods Eng* 1991;31:547–72.
- [47] Belytschko T, Yeh IS. The splitting pinball method for contact-impact problems. *Comput Methods Appl Mech Eng* 1993;105(3):375–93.
- [48] Wriggers P. Finite element algorithms for contact problems. *Archives Comput Methods Eng* 1995;2(4):1–49.
- [49] Wriggers P, Nackenhorst U, editors. *Analysis and simulation of contact problems*. Berlin: Springer-Verlag; 2006.
- [50] Johnson GR, Stryk RA. Symmetric contact and sliding interface algorithms for intense impulsive loading computations. *Comput Methods Appl Mech Eng* 2001;190(35–36):4531–49.
- [51] Benson DJ, Hallquist JO. A single surface contact algorithm for the post-buckling analysis of shell structures. *Comput Methods Appl Mech Eng* 1990;78(2):141–63.
- [52] Chen JS, Chi SW, Lee CH, Lin SP, Marodon C, Roth MJ, et al. A multiscale meshfree approach for modeling fragment penetration into ultra high-strength concrete. Technical Report ERDC/GSL TR-11–35. Vicksburg, MS: U.S. Army Engineer Research and Development Center; 2011. p. 109.
- [53] Osher S, Fedkiw RP. Level set methods and dynamic implicit surfaces. New York: Springer-Verlag; 2002. p. 273.
- [54] Adley MD, Frank AO, Danielson KT, Akers SA, O'Daniel JL. The advanced fundamental concrete (AFC) model. Technical Report ERDC/GSL TR-10–51. Vicksburg, MS: U.S. Army Engineer Research and Development Center; 2010. p. 34.
- [55] Fossum AF, Brannon RM. On a viscoplastic model for rocks with mechanism-dependent characteristic times. *Acta Geotech* 2006;1:89–106.
- [56] Roth MJ, Chen JS, Slawson TR, Boone RN, Ren X, Chi SW, et al. Multiscale RKPM formulation for modeling penetration of an ultra high-strength concrete material. In: Papadrakakis M, Fragiadakis M, Plevris V, editors. *Proceedings of computational methods in structural dynamics and earthquake engineering*. Corfu, Greece; May 26–28, 2011.
- [57] Ortiz M. A constitutive theory for the inelastic behavior of concrete. *Mech Mater* 1985;4(1):67–93.
- [58] Wilkins ML, Guinan MW. Impact of cylinders on a rigid boundary. *J Appl Phys* 1973;44:1200–6.
- [59] Cargile JD. Development of a constitutive model for numerical simulation of projectile penetration into brittle geomaterials. Technical Report ERDC TR-SL-99–11. Vicksburg, MS: U.S. Army Engineer Research and Development Center; 1999. p. 228.
- [60] Hughes TJR, Winget J. Finite rotation effects in numerical integration of rate constitutive equations arising in large deformation analysis. *Int J Numer Methods Eng* 1980;15(12):1862–7.
- [61] Sherburn JA, Hammons MI, Roth MJ. Modeling finite thickness slab perforation using a coupled Eulerian-Lagrangian approach. *Int J Solids Struct* 2014;51(25–26):4406–13.
- [62] Lin SP. A computational framework for the development of a stochastic micro-cracks informed damage model [PhD dissertation]. Los Angeles: University of California; 2014. p. 175.